fluids

MDPI

Article

Header Shape Effect on the Inlet Velocity Distribution in Cross-Flow Double-Layered Microchannel Heat Sinks

Stefano Savino and Carlo Nonino *

Dipartimento Politecnico di Ingegneria e Architettura, Università degli Studi di Udine, 33100 Udine, Italy; stefano.savino@uniud.it

* Correspondence: carlo.nonino@uniud.it

Abstract: Counter-flow double-layered microchannel heat sinks are very effective for thermal control of electronic components; however, they require rather complicated headers and flow maldistribution can also play a negative role. The cross-flow configuration allows a much simpler header design and the thermal performance becomes similar to that provided by the counter-flow arrangement if the velocity distribution in the microchannels is not uniform. The aim of this work is to show the possibility of achieving a favorable flow distribution in the microchannels of a cross-flow double-layered heat sink with an adequate header design and the aid of additional elements such as full or partial height baffles made of solid or porous materials. Turbulent RANS numerical simulations of the flow field in headers are carried out with the commercial code ANSYS Fluent. The flow in the microchannel layers is modeled as that in a porous material, whose properties are derived from pressure drop data obtained using an in-house FEM code. It is demonstrated that, with an appropriate baffle selection, inlet headers of cross-flow microchannel heat sinks yield velocity distributions very close to those that would allow optimal hotspot management in electronic devices.

Keywords: microchannel heat sinks; double-layer; cross-flow; header geometry; maldistribution

Citation: Savino, S.; Nonino, C. Header Shape Effect on the Inlet Velocity Distribution in Cross-Flow Double-Layered Microchannel Heat Sinks. *Fluids* **2022**, *7*, 7. https://doi.org/10.3390/fluids7010007

Academic Editor: Beatrice Pulvirenti

Received: 3 December 2021
Accepted: 20 December 2021
Published: 24 December 2021

1. Introduction

The increasing performance of electronic components requires the dissipation of increasing amounts of heat generated and, consequently, the adoption of more and more efficient, but still small, cooling systems. In this context, the use of liquid-cooled microchannel heat sinks (MCHS) has long been established. In the early 1980s Tuckerman and Pease [1] designed a very compact liquid cooled single-layered microchannel heat sink (SL-MCHS). Since then, a remarkable amount of investigation has been devoted to improving the overall thermal performance of this kind of devices. A comprehensive review can be found in the works of Adham et al. [2] and He et al. [3].

The most common option to increase SL-MCHS performance is to use two layers of microchannels. More than twenty years ago, Vafai and Zhu [4] designed a double-layered microchannel heat sink (DL-MCHS) for electronic cooling with a counter-current flow arrangement. Over the years, it has been demonstrated that double-layered microchannel heat sinks allow to obtain particularly interesting performances in terms of reduction of thermal resistance and control of hotspots. Wei et al. [5] manufactured and tested a DL-MCHS with co-current and counter-current arrangements; they found that the first flow configuration might be more +effective in reducing the hot spot temperature, while the second flow configuration provides a better temperature uniformity, reducing thermal stresses in the heat sink. Levac et al. [6] also compared parallel flow and counter-flow configurations for DL-MCHSs; they found that the counter-flow arrangement provides the lowest thermal resistance, except for low flow rates. More recent scientific literature on this topic includes a large number of optimization studies. Hung et al. [7,8] took into account the effect of thermal properties of different substrate materials and optimized the geometric

parameters to minimize the thermal resistance of DL-MCHSs; they came to the same conclusion as Leng et al. [9] since the best configuration turned out to be the one with different microchannels heights for the bottom and top layers. Wu et al. [10], through a parametric investigation on the thermal performance of DL-MCHSs, found that an improvement of the overall performance at a given pumping power can be obtained if the inlet velocity in the bottom microchannel layer is larger than that in the top one. Shen et al. [11] proposed a novel staggered flow alternation structure in a DL-MCHS and found that the temperature of the substrate can be made quite uniform by increasing the number of staggered flow alternation, with affordable pressure drops. Chamoli et al. [12] optimized an improved DL-MCHS design with truncated microchannels in the top layer and variable cross-sectional shape, providing better temperature uniformity and lower maximum temperature on the bottom wall of the heat sink. Zhou et al. [13] carried out a geometric parameter optimization showing that changing the channel inclination angle, i.e., adopting variable channel heights in the axial direction for top and bottom layers, significantly reduces the thermal resistance. Patel and Mehta [14] and Zhang et al. [15] obtained significant improvement of the overall thermal performance by adopting channels with variable widths in the axial direction and having dense fins with a lesser thickness in the upper layer than in the lower one. Finally, in order to reduce thermal resistance and pumping power, a porous medium was used in DL-MCHSs as an alternative to conventional solid vertical ribs by Wang et al. [16] and Li et al. [17] and in place of the horizontal solid substrate between microchannel layers by Ghahremannezhad and Vafai [18]. A comprehensive review of studies on DL-MCHSs can be found in the work of He et al. [3].

The scientific literature analysis clearly shows the excellent thermal performances of double-layered microchannel heat sinks. Most of the studies on DL-MCHSs, however, only concern parallel- or counter-flow configurations and are based on the hypothesis of a uniform average velocity distribution in all the microchannels, thus not taking into account the performance degradation stemming from the often unavoidable flow maldistribution. Furthermore, the cross-flow configuration, where the flow in the microchannels of the bottom layer is perpendicular to the one in the microchannels of the top layer, was seldom considered.

The cross-flow arrangement was studied by Asnari and Kim [19], who found that to obtain performances comparable to those yielded by the standard counter-flow design, modifications to the basic transverse configuration were needed, such as the subdivision of each layer into quarters with opposite flow directions in each quarter [20]. Tang et al. [21] performed an optimization on a DL-MCHS and came to the conclusion that, for the same pumping power, the counter-flow configuration offers better thermal performances than the cross-flow arrangement.

The present authors have proved that, with a different number of microchannels in the upper layer than in the lower layer, it is possible to achieve, even with cross-flow DL-MCHSs, thermal performances comparable to those provided by counter-flow DL-MCHSs [22]. They have also shown that similar results can be obtained by exploiting the flow maldistribution yielded by appropriately designed headers [23]. In this paper they address the problem of designing headers able to generate the desired type of flow maldistribution, i.e., able to produce an improvement in the performances of the cross-flow DL-MCHSs compared to those that would be yielded by uniform distributions of the microchannel velocities.

2. Motivations and Statement of the Problem

As illustrated in the Introduction, counter-flow double-layered microchannel heat sinks (CF-DL-MCHSs) have been shown to be very effective for thermal control of microchips and prevention of hotspot formation. Each layer of a CF-DL-MCHS consists of a large number of parallel microchannels, with the fluid flowing in the same direction in all the microchannels of the same layer, but in the opposite direction to the flow in the microchannels of the other layer. However, the counter-flow configuration requires rather

complicated headers with two separate inlets and two outlets as shown in Figure 1a, which represents a CF-DL-MCHS with triangular headers [24], vertical cylindrical inlet/outlet ports and a Z type in/out configuration [25], i.e., inlet and outlet ports for the same layer placed on opposite sides. In addition, it is inevitable that part of the outlet header of one of the two microchannel layers overlaps, at least partially, with the inlet header feeding the other microchannel layer and this can result in a significant reduction in actual thermal performance compared to theoretical one. Moreover, flow maldistribution can also play a negative role, as shown by Nonino and Savino [26].

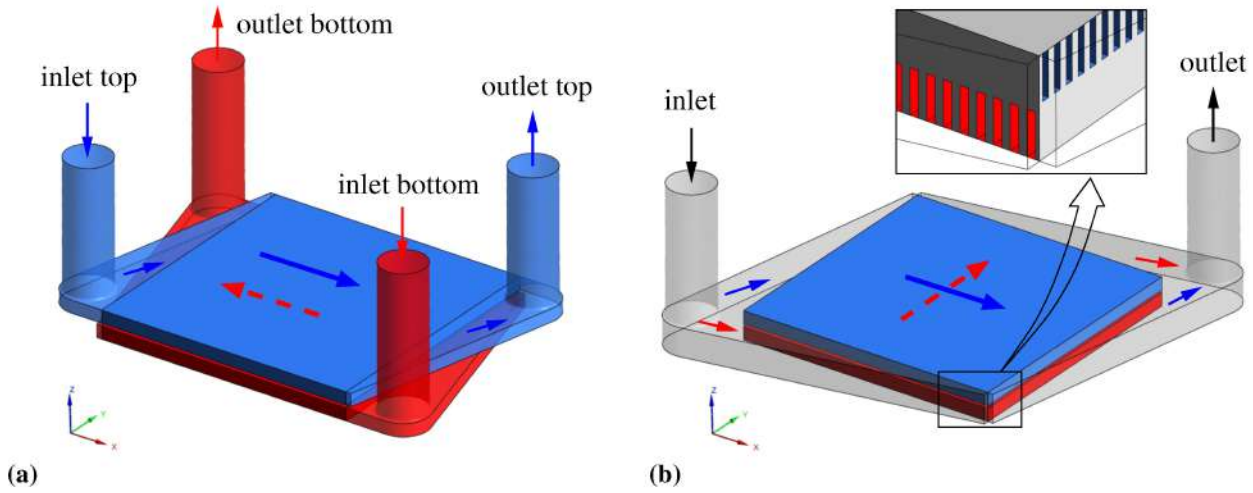

Figure 1. Overall geometry of MCHSs, including headers and inlet/outlet ports: (**a**) counter-flow configuration; (**b**) cross-flow configuration. Box: enlargement of a detail of the microchannels in top and bottom layers.

The disadvantages outlined above could be overcome by the adoption of a cross-flow configuration that would require only one inlet and one outlet header and would not result in heat exchanges between the inlet and outlet current, as can be seen in Figure 1b. Previous investigations carried out by these authors [22], however, have shown that, if the distribution of velocities in the microchannels is uniform, the use of cross-flow double-layered microchannel heat sinks (XF-DL-MCHSs) inevitably results in the formation of a hot spot at the corner opposite to that where the cold fluid inlet is located, as is apparent in Figure 2a, where a three-dimensional map of the temperature distribution on the heated surface of a square microchip cooled with an XF-DL-MCHS is shown as an example. Obviously this determines a significant deterioration of the performance of the MCHS as it causes an increase in thermal resistance

$$R_T = \frac{T_{w,max} - T_{in}}{q_w} \tag{1}$$

which results in a reduction of the maximum heat flux that can be dissipated without exceeding the maximum allowable microchip temperatures. In the previous equation T_{in} is the fluid inlet temperature, $T_{w,max}$ and q_w are the maximum temperature and the heat flow rate on the heated wall of the MCHS. Moreover, a high value of $T_{w,max}$ causes a reduction of the temperature uniformity, which is relevant for thermal stress control and can be quantitatively expressed through the maximum temperature difference on the heated surface

$$\Delta T_{w,max} = T_{w,max} - T_{w,min} \tag{2}$$

where $T_{w,min}$ is the minimum temperature on MCHS-microchip interface.

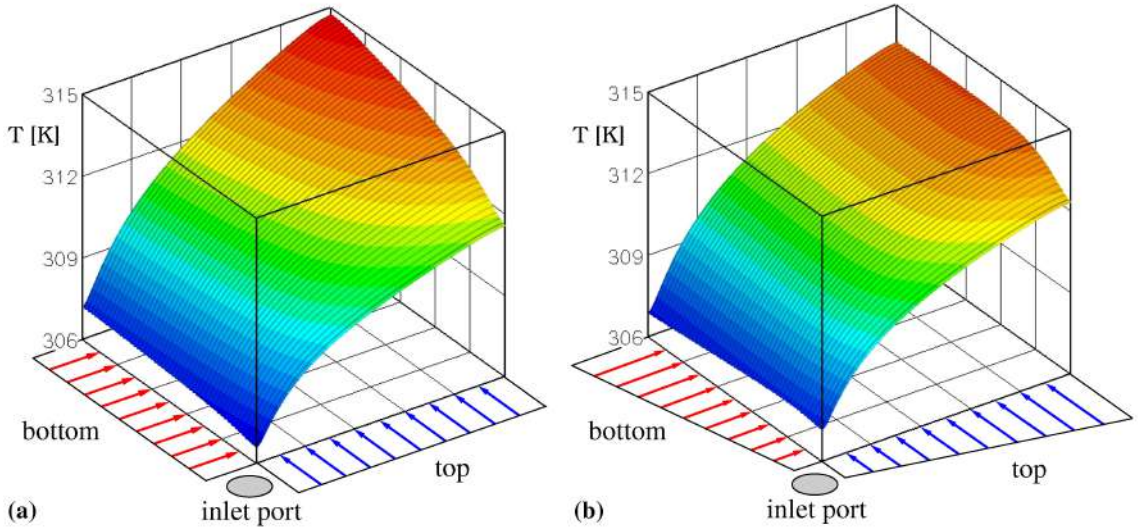

Figure 2. Three-dimensional temperature maps on the heated surface of a square microchip cooled with a cross-flow DL-MCHS: (**a**) uniform microchannel velocity distribution; (**b**) microchannel velocity distribution varying linearly along the inlet sides.

The authors also showed that if the microchannel velocity distribution in the XF-DL-MCHS is not uniform, but is such that the microchannels where velocities are the highest are located near the MCHS sides opposite to the inlet port and close to the outlet one, even an XF-DL-MCHS can achieve a thermal resistance and a temperature uniformity comparable to those produced by an CF-DL-MCHS, as can be seen by looking at Figure 2b, where, with reference to the same test case of Figure 2a the hotspot has been mitigated [23]. The best results are obtained if the microchannel velocity varies linearly along the inlet sides as shown schematically in Figure 2b. Therefore, an investigation has been conducted to find out which features of the inlet header can induce a flow maldistribution that is as close as possible to the desired linear trend. Headers with a shape similar to that shown in Figure 1b can produce a flow maldistribution suitable for the purpose only when the fluid velocity is high enough. In the case of low flow rates, however, the effect is insufficient to ensure adequate hotspot control. Therefore, the objective of this work is to study the possibility of obtaining an adequate flow maldistribution with the aid of additional elements within the header such as full or partial height baffles made of solid or porous materials. Only the velocity fields in headers are analyzed in this work to get an indication of the microchannel velocity distribution, while the effects of the flow maldistribution on the thermal fields in MCHSs will be analyzed in a subsequent paper.

3. Mathematical Model

In order to keep the computational effort within acceptable limits, the flow in the two overlapping layers of orthogonal microchannels was treated as that in two layers of a porous medium since the only results of interest were the velocity distributions on the plane where the microchannel inlets are located and not the actual velocity field inside the microchannels.

3.1. Governing Equations

The steady state incompressible constant property flow in the MCHS, which is turbulent in the inlet and outlet ports and in the headers, is governed by the continuity and Navier-Stokes equations, written in a form suitable for the application of a RANS turbulence model

$$\frac{\partial v_j}{\partial x_j} = 0 \tag{3}$$

$$\rho\frac{\partial(v_i v_j)}{\partial x_j} = +\frac{\partial}{\partial x_j}\left[(\mu+\mu_t)\left(\frac{\partial v_i}{\partial x_j}+\frac{\partial v_j}{\partial x_i}\right)\right] - \frac{\partial p}{\partial x_i} + S_i \tag{4}$$

where v_i are the mean velocity components, x_i are the Cartesian coordinates, p is the deviation from the hydrostatic pressure, ρ is the density, μ and μ_t are the molecular and turbulent viscosity, respectively. Since parts of the domain correspond to porous media or are treated as such, the source term S_i is included in Equation (4) to allow modeling of the flow in these materials. According to the Einstein notation adopted here, the occurrence of an index variable twice in a single term implies summation.

The turbulence model used in this work is the Realizable $k-\epsilon$ model summarized by the following set of equations

$$\rho\frac{\partial(v_j k)}{\partial x_j} = \frac{\partial}{\partial x_j}\left[\left(\mu+\frac{\mu_t}{\sigma_k}\right)\frac{\partial k}{\partial x_j}\right] + G_k - \rho\varepsilon \tag{5}$$

$$\rho\frac{\partial(v_j \varepsilon)}{\partial x_j} = \frac{\partial}{\partial x_j}\left[\left(\mu+\frac{\mu_t}{\sigma_\varepsilon}\right)\frac{\partial \varepsilon}{\partial x_j}\right] + \rho C_1 S\varepsilon - \rho C_2\frac{\varepsilon^2}{k+\sqrt{\nu\varepsilon}} \tag{6}$$

$$C_1 = max\left[0.43, \frac{\eta}{\eta+5}\right],\ \eta = S\frac{k}{\varepsilon} \tag{7}$$

$$\mu_t = \rho C_\mu \frac{k^2}{\varepsilon} \tag{8}$$

where k is the turbulent kinetic energy, ϵ is the rate of dissipation of turbulent kinetic energy, G_k is the generation of turbulent kinetic energy, S is the modulus of the mean rate-of-strain tensor and C_μ is a function of the mean strain and rotation rates and of the turbulent fields k and ε, while $\sigma_k = 1.0$, $\sigma_\varepsilon = 1.2$ and $C_2 = 1.9$ are the typical constants of the $k-\epsilon$ model [27].

3.2. Porous Media Treatment

The source term S_i used in Equation (4) to account for the effect of porosity is calculated using the relationship based on the Forchheimer equation [28]

$$S_i = -\left(\frac{\mu}{\alpha_i}v_i + C_i\frac{1}{2}\rho|\mathbf{v}|v_i\right) \tag{9}$$

where α_i and C_i are the permeability and the inertial resistance factor in the i-th direction and $\mathbf{v}$ is the velocity vector. In the the porous layer, $\mathbf{v}$ and v_i should be considered superficial velocities.

In the present study, the flow in the microchannels of a layer of the MCHSs is modeled as the flow in a porous material in which the permeability in one direction is much larger than that in the other two orthogonal directions. Therefore, the value of the permeability α_i in the flow direction is calculated together with that of the inertial resistance factor C_i from pressure drop data for flows in microchannels similar to those forming the MCHS, while a very small value of α_i is assumed in the directions perpendicular to the microchannel solid walls. Instead, to model the flow in the porous baffles, the values of α_i and C_i were taken from literature data.

4. Numerical Simulations

Numerical simulations were conducted using the FVM commercial code ANSYS Fluent [29] with the aim of verifying the effect on the uniformity of the microchannels inlet velocity distribution resulting from changes to the basic geometry of the inlet header in a cross-flow DL-MCHS. The considered geometry variations consist in the insertion in the inlet header of a baffle of suitable shape, possibly porous or of partial height, with the purpose of directing the flow towards the parts of the DL-MCHS farthest from the inlet port. In all the numerical simulations, water was assumed as the working fluid since this

coolant is often used in MCHS applications [12,14,20,25]. The following properties of water at a temperature of 300 K were used: $\rho = 995.6$ kg/m^3, $\mu = 0.000854$ kg/(m * s). In all the test cases, the iterative solution of the model equation was obtained with an absolute tolerance on the residuals set at 10^{-6} for all unknown variables.

4.1. Computational Domains and Boundary Conditions

In this work reference is made to a cross-flow DL-MCHS with 50 microchannel per layer having a height equal to 0.5 mm and width of 0.10 mm. The thickness of the walls that separate adjacent microchannels of the same layer and the thickness of the solid material between the two layers of microchannels are both assumed equal to 0.10 mm. Thus, the footprint of the DL-MCHS has a size of 10×10 mm^2. The height of the fluid passages in the headers is equal to 1.10 mm. The lengths of the two cylindrical inlet and outlet ports are 5.0 mm and 20.0 mm, respectively.

For the purposes of this study, the properties of the solid are irrelevant. However, in actual devices, silicon, copper or aluminum is used as the heat sink material. Advanced manufacturing technologies allow the application of porous media also in MCHSs. The porous baffle proposed in this study could be a sintered metallic medium, made from copper or stainless steel powders [18,30–32].

The overall geometry of the computational domain is shown in Figure 1b and includes the two layers of microchannels in cross-flow represented in red and blue in the figure and modeled as porous media, the inlet and outlet headers, and two sections of the inlet and outlet piping. The dimensional details that can be deduced from a plan view of the MCHS are shown in Figure 3a, where all the dimensions are in millimeters and the gray square corresponds to the area occupied by the layers of microchannels which were considered as porous media layers of equal height. Since the width of the microchannels is equal to the thickness of the separation walls, the porosity is 50% and the equivalent velocity in the microchannels, which is the parameter of interest in this work, is calculated as twice the average surface velocity at the position corresponding to the microchannel entrance on the internal boundary that forms the interface between the porous layer and the header. The two porous layers are separated by a distance of 0.10 mm, corresponding to the thickness of the wall between the two microchannel layers.

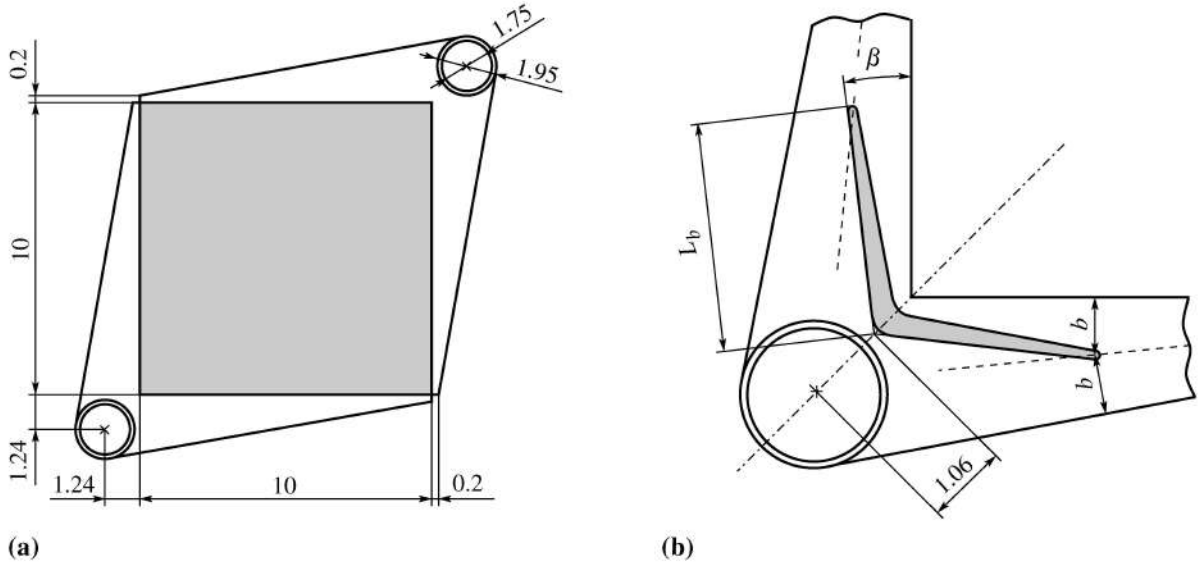

Figure 3. Plan view and dimensions in millimeters of the computational domain: (**a**) basic geometry; (**b**) angled baffle position in the inlet header.

In addition to the basic geometrical configuration described above, several instances of the case where a symmetrical baffle, which may be made of solid or porous material, is

inserted into the header were also analyzed. With reference to Figure 3b, the position of the vertex of the baffle angle was kept fixed, while different values of the angle β and of the half-length L_b of the baffle were considered. However, the combinations of these values were chosen in such a way that the baffle ends are always placed in a position at the same distance b from the plane where the microchannel inlets are located and from the solid wall on the opposite side, as shown in Figure 3b. The minimum and maximum thickness of the baffles are equal to 0.12 and 0.40 mm, respectively. The following groups of test cases were considered:

- no baffle in header (Case: NB);
- full height solid baffle with half-length $L_b = 1.5$, 3.0 and 4, 5 mm (Cases: S-L1, S-L2, S-L3);
- partial height solid baffle with (i) half-length $L_b = 3.0$ mm and heights equal to 75% and 90% of the height of the header fluid passage (Cases: C1-L3, C2-L3) and with (ii) half-length $L_b = 4.5$ mm and heights equal to 75% and 90% of the height of the header fluid passage (Cases: C1-L4, C2-L4);
- full height porous baffle with half-length $L_b = 6.5$ mm and different permeability combinations in three baffle sections as detailed in Section 5.4 (Cases: P1, P2, P3).

The boundary conditions applied for solution of the governing equations are: specified velocity on inlet boundaries, pressure boundary conditions on outlet boundaries and enhanced wall treatment (as implemented in ANSYS Fluent) on solid boundaries. More in detail, three values of the average microchannel velocity u_{ave} were considered, namely, 0.5, 1.0 and 2.0 m/s corresponding to values of $u_{in} = 1.04$, 2.08 and 4.16 m/s in the inlet pipes and Reynolds numbers equal to 2120, 4241 and 8482, respectively. Slip conditions are specified on the lateral, top and bottom boundaries of the porous layers.

4.2. Porous Coefficients

For the porous layers that replace the microchannels, the porous coefficients α_i and C_i that appear in Equation (9) were derived based on the pressure drop data for microchannels of the same height, width and length as those considered here, obtained using an in-house FEM code for the solution of the parabolized form of the Navier-Stokes equations [33]. The combinations of microchannel average velocity and corresponding pressure drop are shown in Table 1, while the porous coefficients, computed according to [28], are $\alpha_i = 3.634 \times 10^{-10}$ m^2 and $C_i = 374.1$ m^{-1} if the subscript i identifies the flow direction and $\alpha_k = 10^{-14}$ m^2 and $C_k = 10^7$ if $k \neq i$.

Table 1. Pressure drop in microchannels of height, width and length equal to 0.5, 0.1 and 10 mm for different microchannel average velocities.

u_j [m/s]	0.25	0.5	1.0	1.5	2.0	2.5	3.0	3.5
Δp [Pa]	2965	5988	12,211	18,675	25,360	32,285	39,421	46,830

The porous coefficients for the different parts of the baffle in cases P1, P2 and P3 are set based on literature data, as detailed in Section 5.4.

4.3. Domain Discretization and Validation

The computational domains have been discretized using tetrahedral cells in the parts corresponding to the ports and headers and hexahedral cells (parallelepipeds) in the parts of the domain corresponding to the microchannel layers (porous medium). At the common interfaces, the grids of the two types are non-conformal. An inflation layer, with hexahedral cells of increasing thickness with the distance from the wall, was generated at the solid surfaces in the parts of the domain where the flow is turbulent, as can be seen in Figure 4, which illustrates the structure of one of the computational grids. In the porous layers, represented in red and blue in the figure, the grid is very coarse in the flow direction since

only the pressure drop in these layers affects the flow in the headers and not the details of the velocity field.

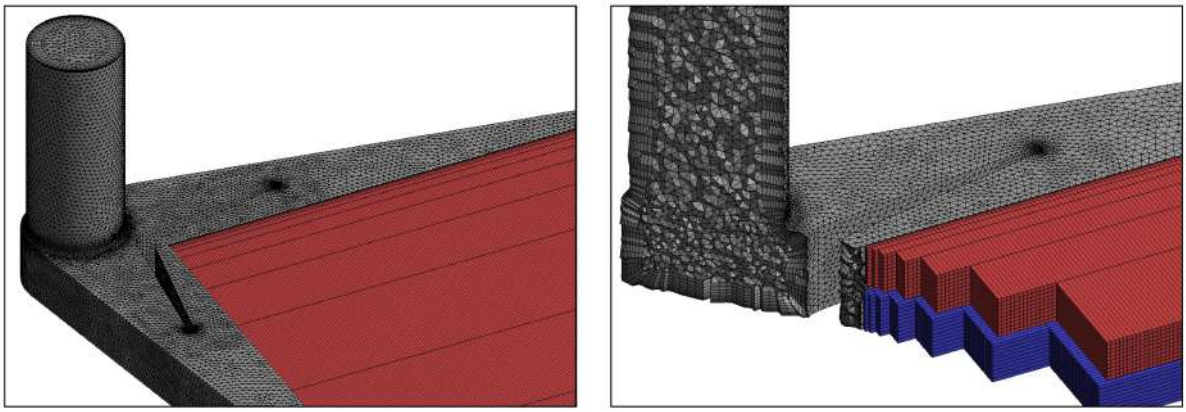

Figure 4. Mesh details showing the structure of the computational grid selected for a representative test case: (**a**) basic geometry; (**b**) angled baffle position in the inlet header.

A grid independence study was conducted with reference to case S-L3 (header with full height solid baffle of half-length $L_b = 4.5$ mm) for an average microchannel velocity $u_{ave} = 2$ m/s, which is the highest among those considered in this investigation. Five grids, named G1, G2, G3, G4 and G5, were used, with a number of cells equal to 454,429; 984,132; 1,591,851; 2,133,265 and 2,612,852, respectively.

The effect of refining the grid was verified with reference to the changes in the two flow features that are most relevant for this study, namely, the pressure drop in the MCHS (with the exclusion of the cylindrical inlet and outlet ports) and the microchannel average velocity distribution. The values of the following parameters are reported in Table 2 as computed from the results obtained with the five grids considered:

- the percentage variation of the pressure drop Δp_K between two successive grids

$$\delta_p = \frac{\Delta p_{K+1} - \Delta p_K}{\Delta p_K} \times 100 \tag{10}$$

- the percentage mean deviation of the microchannel velocity distribution $u_{K,j}$ in each layer between two successive grids

$$\delta_u = \frac{1}{50} \sum_{j=1}^{50} \frac{\left| u_{K+1,j} - u_{K,j} \right|}{u_{K,ave}} \times 100 \tag{11}$$

where subscripts K and $K+1$ identify two successive grids and $K = 1, 2, 3, 4$. The values of δ_u reported in Table 2 are the average of those obtained for the top and bottom layers.

Table 2. Percentage variation of the pressure drop δ_p and percentage mean deviation of the microchannel velocity distribution δ_u between two successive grids.

	G2 vs. G1	G3 vs. G2	G4 vs. G3	G5 vs. G4
δ_p	1.89%	0.77%	0.42%	0.30%
δ_u	2.61%	0.87%	0.51%	0.25%

As can be seen, the changes of both parameters are only marginal when going from grid G4 to grid G5. Therefore, grid G4 with 2,133,265 cells and a maximum cell size in the non-porous part of the domain equal to 0.10 mm was adopted for this test case. With this grid, the maximum value of the dimensionless distance from the wall y^+ is 5.15, while

the average value is 2.06. Grids based on the same maximum cell size and with a similar number of cells were used for all the other test cases.

No experimental data are available for the validation of this problem. However, this should not be of too much concern because the purpose of this work is not the detailed simulation of a real case, but it is just to demonstrate the validity of a method to obtain a desired microchannel velocity distribution. Moreover, the reliability of the ANSYS Fluent code for the accurate solution of single-phase turbulent flow problems is already well established. In fact, in the past several researchers have satisfactorily used this code with the same turbulence model adopted in here (Realizable $k-\epsilon$ model) for the numerical analysis of the flow in different types of heat sinks [34–36].

5. Numerical Results

As already stated, the objective of this work is to obtain an adequate maldistribution in the headers of cross-flow DL-MCHSs to reduce the intensity of the hotspot and, in turn, to limit the thermal resistance. Therefore, in this section, results of numerical simulations are shown in terms of flow maldistribution in the 50 microchannels pertaining to the top and bottom layers of the heat sink. Since the layers are treated as porous media, the velocity u_j in the j-th microchannel is assumed to be equal to twice the superficial velocity, averaged in the vertical direction z, calculated in the porous medium at the spatial location corresponding to the centerline of the microchannel. In each layer of the XF-DL-MCHS, the microchannels are numbered starting from the side close to the inlet port of the header. Thus, the channel number j increases in the same direction as the coordinate axes: x for the top layer and y for the bottom layer. As mentioned in Section 2, a flow maldistribution with a positive effect on the thermal resistance exhibits low velocities in channels close to the inlet port (i.e., channel number j close to 1) and high velocities in those farthest form the inlet port (i.e., channel number j close to 50). In order to compare results for different flow rates, velocities are normalized with the average microchannel velocity u_{ave}. The most significant features of the flow field affecting the velocity distribution in the microchannels are highlighted in this section by showing pathlines in the heat sink inlet header.

5.1. Header without Baffle (Case: NB)

The first simulations were carried out considering the basic header geometry described in Figure 3a, without any baffle. In Figure 5a, normalized velocity distributions in the microchannels are shown for three different average microchannel velocity values u_{ave} for top and bottom layers; as a reference, the constant value $u_j/u_{ave} = 1$ corresponds to the case of flow without maldistribution. As can be seen, the header geometry itself is able to generate a thermally advantageous maldistribution, as the velocities are higher in the channels farthest from the inlet port. Velocities increase monotonically and reach their maximum value at the last microchannel inlet; distributions are very similar in top and bottom layers. The effect of the average microchannel velocity u_{ave} is remarkable: as u_{ave} increases, the maldistribution is amplified in terms of maximum and minimum normalized velocity values.

The velocity distributions in Figure 5a can be justified by looking at Figure 5b, where pathlines in the inlet header are depicted for $u_{ave} = 1.0$ m/s, i.e., the intermediate value among those considered in this work. Walls are displayed as shaded gray surfaces.The heat sink header is fed through the vertical inlet duct; as a consequence, the fluid impinges on the lower surface of the header and is then distributed in the two microchannel layers. Two main fluid paths can be identified: the fluid entering the front part of the header flows quite smoothly towards the microchannel layers, while the fluid entering the rear part of the header is pushed forward by the side walls, generating a strong recirculation near the inlet port zone. Due to this recirculation, the fluid is diverted towards the ends of the manifold, increasing the velocity in the microchannels farthest from the inlet port, as seen in Figure 5a. On the right-hand side of Figure 5b, the streamlines rise to enter the top layer of microchannels in the upper region of the header, while on the left-hand

side the streamlines point downwards to enter the bottom layer in the lower region of the manifold; this is the reason for the slightly different top and bottom flow maldistributions in Figure 5a. Recirculation becomes more intense as the average velocity u_{ave} increases, thus justifying a more pronounced flow maldistribution.

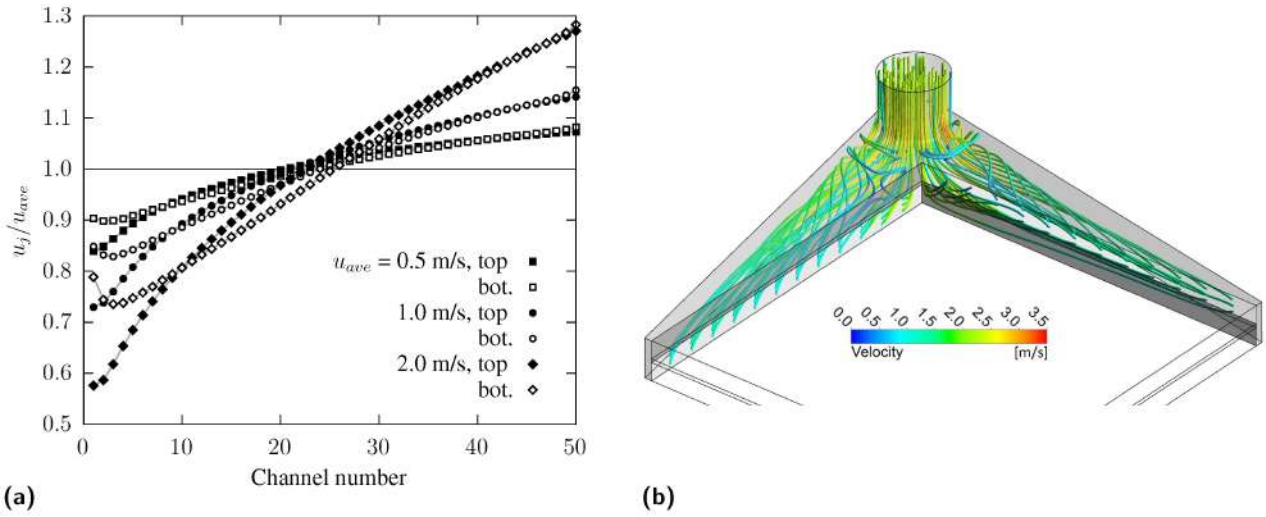

Figure 5. Header without baffle: (**a**) normalized velocity distributions obtained with different average velocities u_{ave} for top and bottom layers; (**b**) pathlines in the inlet header for u_{ave} = 1.0 m/s, colored by velocity magnitude.

5.2. Header with Solid Baffle (Cases: S-L1, S-L2, S-L3)

The basic header geometry can induce a remarkable maldistribution only when the flow rate is high enough, while in the case of small average velocities the flow maldistribution is not sufficient to ensure a good hotspot control. For this reason, a symmetrical baffle of solid material, whose geometry has already been described in Section 4.1, is placed in the inlet header. To assess the effect of the baffle half-length L_b on the velocity field, three different values were analyzed as can be seen in Figure 6a: L_b = 1.5 mm (case S-L1, colored in red), L_b = 3.0 mm (case S-L2, colored in green) and L_b = 4.5 mm (case S-L3, colored in blue).

In Figure 6b–d normalized velocity distributions in the microchannels for the three different values of L_b are shown for u_{ave} = 0.5, 1.0 and 2.0 m/s, respectively. As a reference, the normalized microchannel velocity distributions for the case without baffle (case NB) are included in the figure; the dashed line refers to the top layer, while the dotted line pertains to the bottom layer. As expected, the baffle significantly increases the flow maldistribution in the microchannels: velocity profiles show low velocities near the inlet, where microchannel layers are shielded by the baffle, followed by a steep increase just past the baffle ends. The sharp velocity rise zone moves farther from the inlet port for larger values of L_b. Velocities increase monotonically only for case S-L1. When the baffle length increases a strong peak appears, with velocity values similar (for small flow rates) or even higher (for high flow rates) than those in the last microchannels of the layers. As already pointed out for the case without baffle, the effect of average velocity u_{ave} is remarkable: as u_{ave} increases, the flow maldistribution is amplified in terms of maximum and minimum normalized velocity values. Despite having similar trends, the distributions are slightly different in top and bottom layers.

Pathlines in the inlet header pertaining to u_{ave} = 1.0 m/s are represented for the minimum and maximum values of L_b, i.e., 1.5 mm and 4.5 mm, in Figure 7a and Figure 7b, respectively. The baffle walls are shaded in dark gray. The baffle guides the fluid, fed through the vertical inlet duct, towards the ends of the header; velocities are very low in the area shielded by the baffle, corresponding to the microchannels near the inlet port, and become very high at the extrados of the baffle, where the flow passage area reaches

its minimum value. Wide recirculation regions form at the trailing edges of the baffle, causing valleys and consequent peaks in the curve, with the steep velocity increase already described while commenting Figure 6b–d. For larger values of L_b, the recirculation becomes more intense and velocities at the baffle extrados are much higher (red colored pathlines in Figure 7b), leading to the non-monotonic velocity distributions shown in Figure 6b–d.

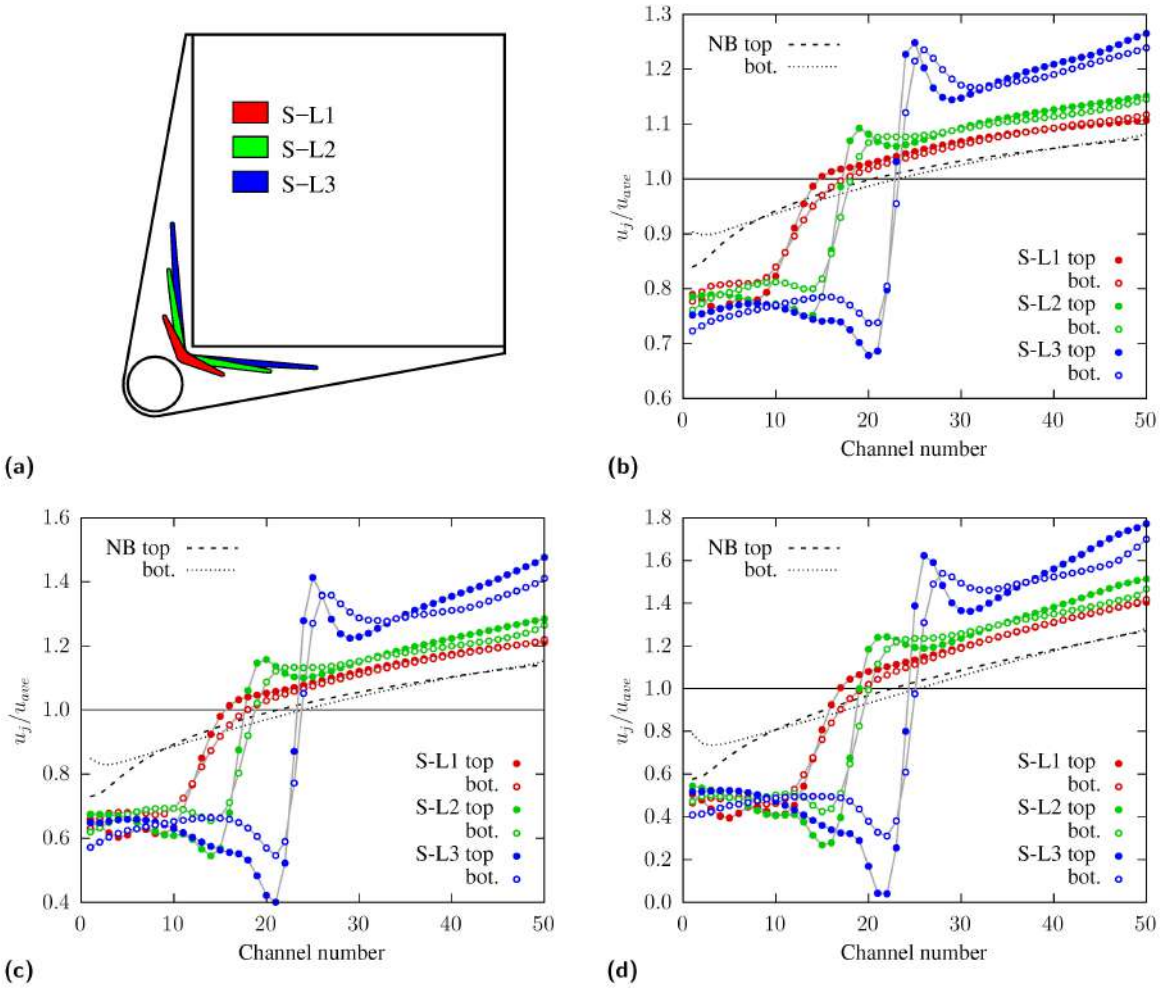

Figure 6. Header with solid baffle: (**a**) sketch of the inlet header with baffles of different lengths; normalized velocity distributions for top and bottom layers obtained with different average velocities: (**b**) $u_{ave} = 0.5$ m/s, (**c**) $u_{ave} = 1.0$ m/s, (**d**) $u_{ave} = 2.0$ m/s.

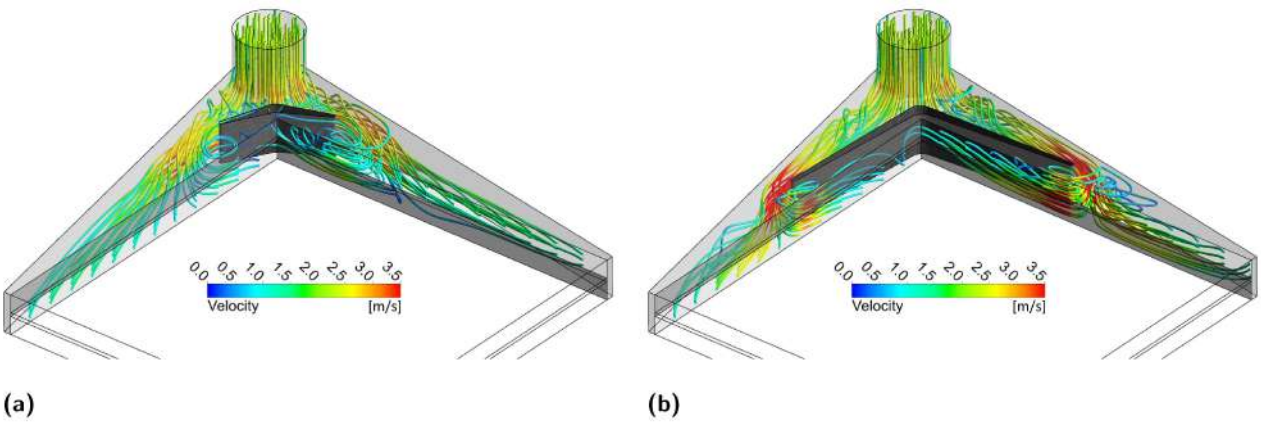

Figure 7. Header with solid baffle: pathlines in the inlet header for $u_{ave} = 1.0$ m/s, colored by velocity magnitude for (**a**) $L_b = 1.5$ mm (case S-L1) and (**b**) $L_b = 4.5$ mm (case S-L3).

5.3. Header with Cut Baffle (Cases: C1-L3, C2-L3, C1-L4, C2-L4)

The solid baffles described in the previous subsection are capable of producing a marked maldistribution. However, they generate valleys and peaks in the curves that make the velocity distribution far from the linear trend, which is, from the hotspot control point of view, the most effective pattern. For this reason, partial height solid baffles are analyzed in this subsection, with the aim of obtaining smoother velocity distributions. In order to asses the effect of different partial baffle heights, baffles are cut at the 75% (cases referred to as C1) and 90% (cases referred to as C2) of the height of the header fluid passage. Partial height baffles offer less resistance to the fluid flow than solid ones, generating a milder flow maldistribution. In order to compensate for this effect, two large values of the baffle half length were considered as can be seen in Figure 8a: $L_b = 4.5$ mm (case L3, colored in blue) and $L_b = 6.0$ mm (case L4, colored in red).

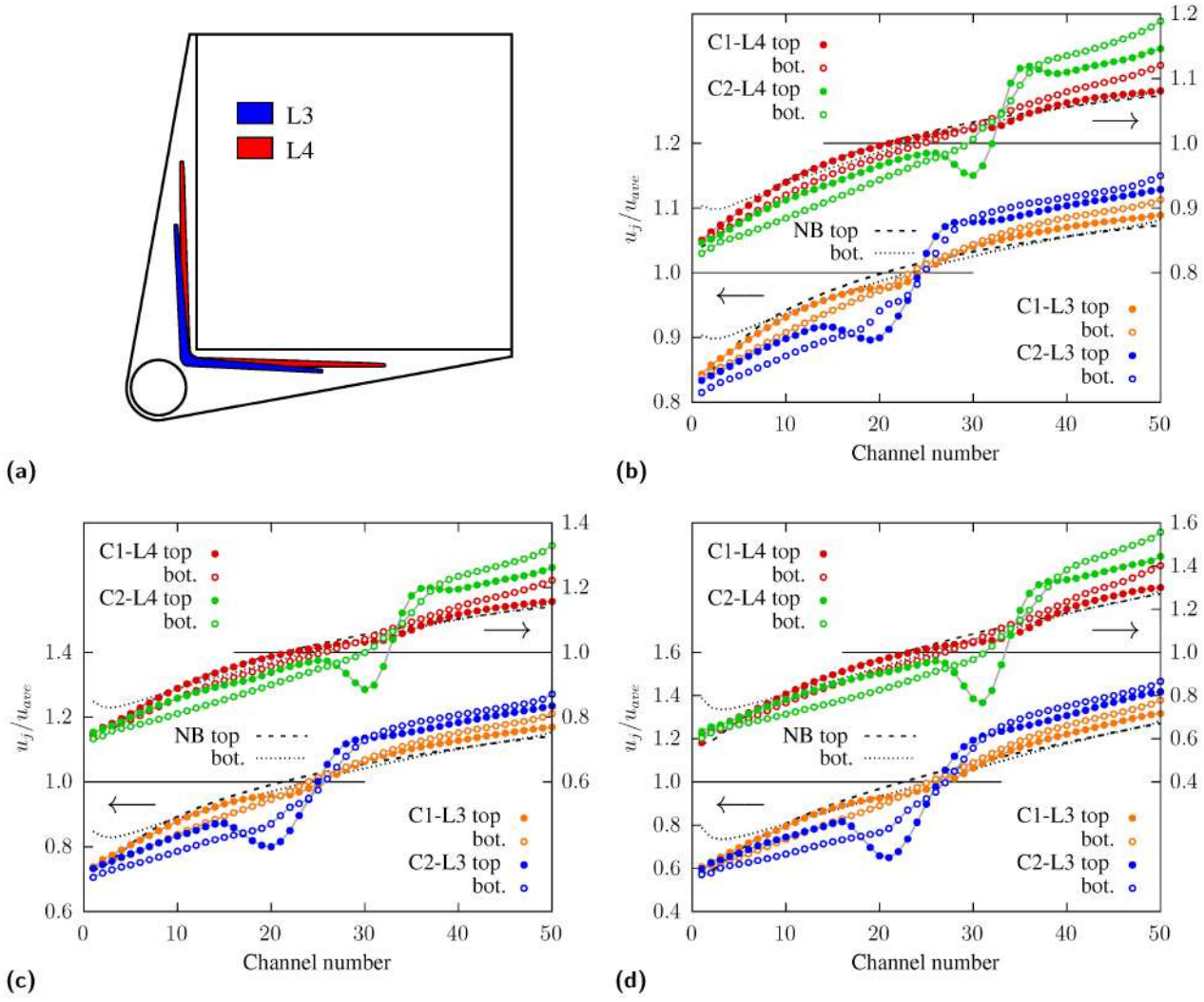

Figure 8. Header with cut baffle: (**a**) sketch of the inlet header with baffles of different lengths; normalized velocity distributions for top and bottom layers obtained with different average velocities: (**b**) $u_{ave} = 0.5$ m/s, (**c**) $u_{ave} = 1.0$ m/s, (**d**) $u_{ave} = 2.0$ m/s.

In Figure 8b–d normalized velocity distributions in the microchannels for the two different values of baffle height and two different values of baffle length are shown for $u_{ave} = 0.5$, 1.0 and 2.0 m/s, respectively. Comparing Figure 6b–d and Figure 8b–d it is apparent that, for the same baffle length (cases L3), the partial height baffle generates a less pronounced but more regular flow maldistribution, especially for the smaller partial height (cases C1). For the larger value of partial height (cases C2), velocity profiles show peaks and

valleys, especially for the top layer, although less pronounced than in the case of full-height baffles. The effect of the average velocity u_{ave} is still remarkable: as u_{ave} increases, the flow maldistribution is amplified. For C1 cases, i.e., a smaller baffle height, the velocity distributions for top and bottom layers are very similar and close to those without baffle.

The effect of considering partial height baffles on the flow field is illustrated in Figure 9, where pathlines in the inlet header pertaining to $u_{ave} = 1.0$ m/s are depicted for the two extreme geometrical configurations: case C1-L3 in Figure 9a, referring to the shortest baffle with the smallest height, and case C2-L4 in Figure 9b, referring to the longest baffle with the largest height. The baffle walls are shaded in dark gray. It can be clearly seen that a fraction of the fluid entering the header bypasses the baffle through its top opening. The fluid flow is much smoother and velocities are lower for case C1-L3 than for case C2-L4, where high velocities and a strong recirculation can be seen at the baffle leading edges.

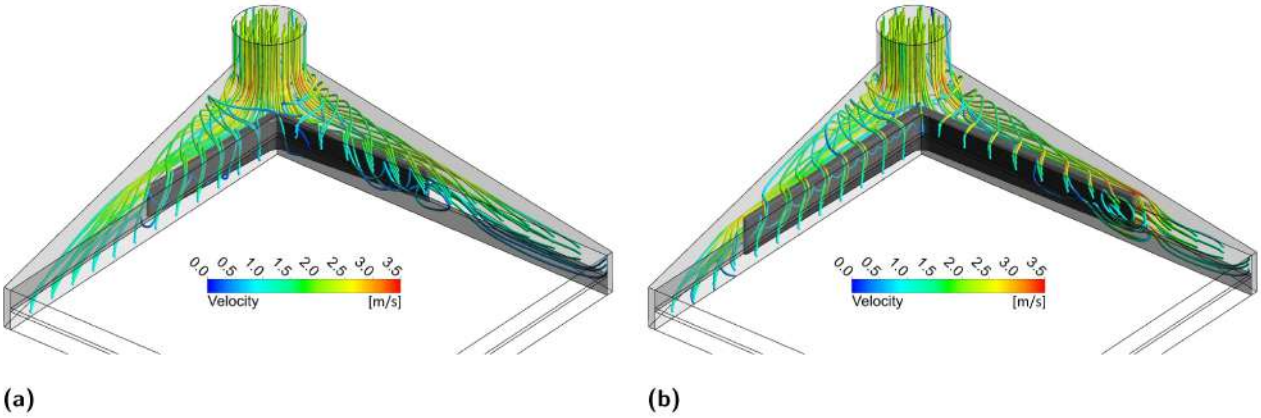

Figure 9. Header with cut baffle: pathlines in the inlet header for u_{ave} = 1.0 m/s, colored by velocity magnitude for (**a**) $L_b = 4.5$ mm and 75% cut height (case C1-L3) and (**b**) $L_b = 4.5$ mm and 90% cut height (case C2-L4).

5.4. Header with Porous Baffle (Cases: P1, P2, P3)

Although partial height baffles produce a smoother flow maldistribution than full height ones, the difference between maximum and minimum microchannel velocities is much smaller and not large enough for an efficient hotspot control. In order to obtain large velocity differences and, at the same time, velocity distributions as close as possible to a linear trend, the full height baffle with the largest value of half-length $L_b = 6.0$ mm was replaced with a baffle made of porous material. The porous baffle is divided into three sections, identified by different shades of gray in Figure 10a and characterized by different permeabilities. The three baffle sections have lengths equal to 2.05 mm if measured as shown in Figure 10a.

Three different combinations of the permeability of the baffle sections, referred to as P1, P2 and P3, were considered to verify the possibility of obtaining smooth microchannel velocity distributions with large differences between maximum and minimum velocities. The permeability of each section increases from the baffle center to its ends. The baffle section closer to the inlet port has the lowest permeability, providing a high flow resistance, while the sections at the baffle ends have the highest permeability, thus providing a small flow resistance. The value of the permeability α_i for each baffle section was chosen based on literature data [37,38], while the inertial resistance factor C_i was calculated using the expression [30,39]

$$C_i = 2\frac{C_F}{\sqrt{\alpha_i}} \tag{12}$$

where C_F is the Forchheimer's constant, assumed equal to 0.3 in this work [17,32,40]. Since the porous material can be considered isotropic, the same values of α_i and C_i were used for all di-

rections. The permeability values adopted in the different combinations are reported in Table 3 and fall within the ranges proposed in the literature for microchannel applications [31,37].

Table 3. Permeability values α_i [m^2] for the three porous baffle sections for combinations P1, P2 and P3.

Combination	Low Permeability	Medium Permeability	High Permeability
P1	3.0×10^{-12}	6.0×10^{-11}	6.0×10^{-9}
P2	1.0×10^{-14}	8.0×10^{-12}	2.7×10^{-9}
P3	1.0×10^{-14}	1.0×10^{-14}	2.0×10^{-10}

As can be seen in Table 3, the permeability decreases from case P1 to case P3 and the low permeability section for P2 and both the low and medium permeability sections for P3 are, basically, solid.

In Figure 10b–d normalized velocity distributions in the microchannels for the three different porosity combinations are reported for $u_{ave} = 0.5$, 1.0 and 2.0 m/s, respectively. As expected, the flow maldistribution becomes more and more pronounced moving from case P1 (larger permeabilities in the baffle sections) to case P3 (smaller permeabilities in the baffle sections). The differences between minimum and maximum normalized velocities are similar to those yielded by solid baffles, but profiles are much smoother and very weak peaks and valleys in the curve only appear for high flow rates. Velocities increase almost monotonically and reach their maximum values at the last microchannel inlet. There is almost no difference between top and bottom distributions, suggesting that the porous baffle has a strong smoothing effect on the flow field. Changes in the slope of the velocity trends are related to the transition between different porous sections of the baffle. The last steep increase in velocity, which is particularly strong for the P3 combination, is located at the baffle ends, as was the case for the solid baffle. Once again, the flow maldistribution is amplified as the average microchannel velocity increases.

The effect of the porous baffle on the flow field is illustrated in Figure 11, where pathlines in the inlet header, pertaining to $u_{ave} = 1.0$ m/s are shown for the two extreme porous combinations, P1 (Figure 11a) and P3 (Figure 11b). The pathlines are much more regular than those for solid or cut baffle cases and recirculation zones are much smaller, and almost unnoticeable for case P1. Comparing Figure 7b and Figure 11b, it can be clearly seen that the velocities at the baffle extrados are much lower in the porous case, even if the solid baffle is longer ($L_b = 4.5$ mm for case S-L3 in Figure 7b and $L_b = 6.5$ mm for case P3 in Figure 11b). All these considerations explain why velocity distributions shown in Figure 10b–d are more regular and closer to a linear trend, especially for the low porosity cases P1 and P2.

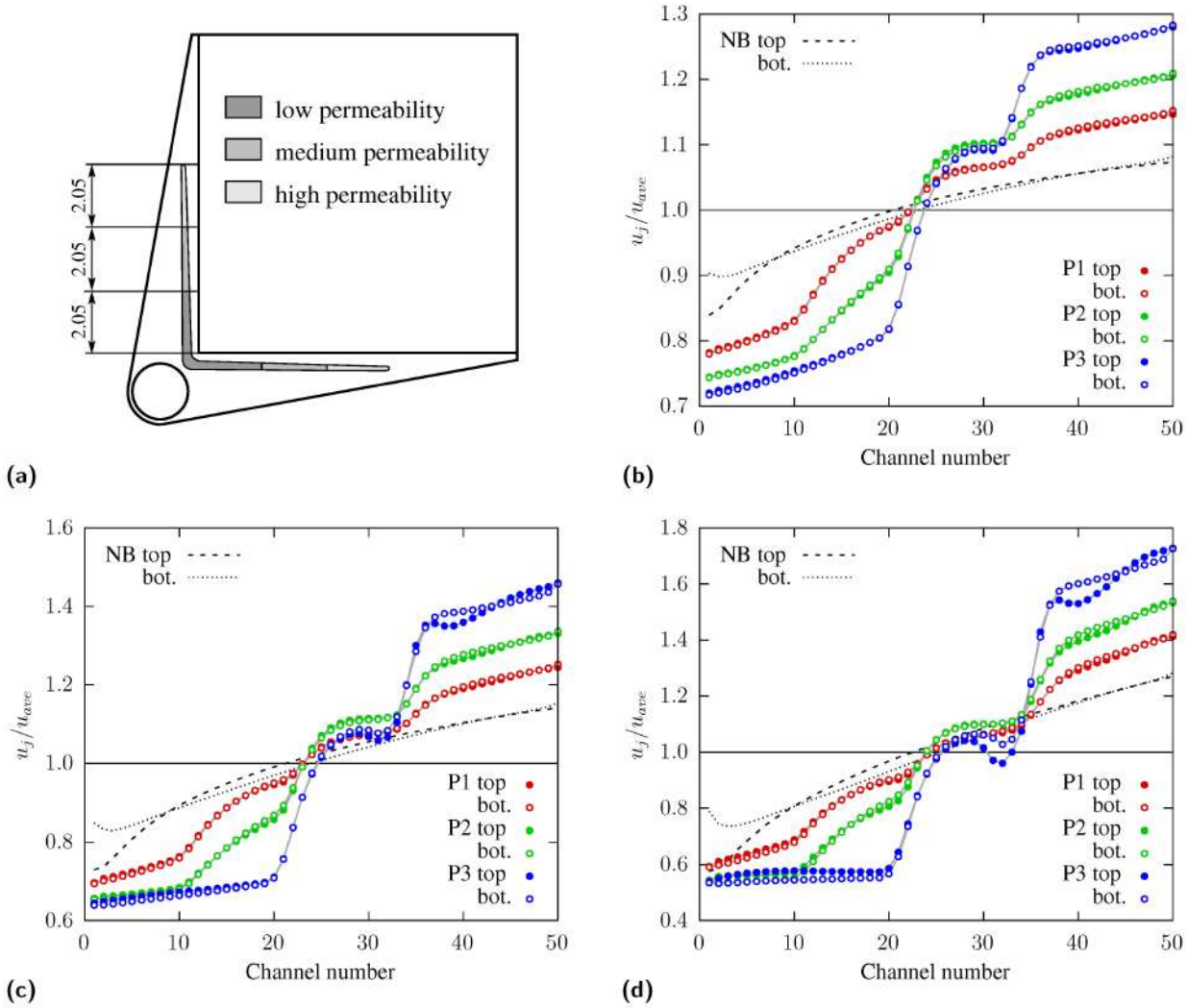

Figure 10. Header with porous baffle: (**a**) sketch of the inlet header and baffle with different porous sections; normalized velocity distributions for top and bottom layers obtained with different average velocities: (**b**) $u_{ave} = 0.5$ m/s, (**c**) $u_{ave} = 1.0$ m/s, (**d**) $u_{ave} = 2.0$ m/s.

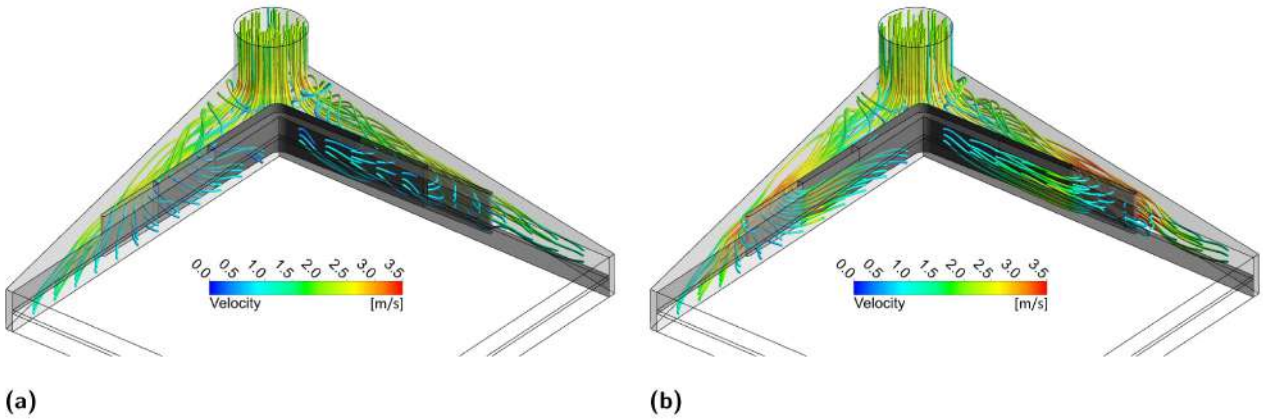

Figure 11. Header with porous baffle: pathlines in the inlet header for $u_{ave} = 1.0$ m/s and $L_b = 6.0$ mm, colored by velocity magnitude for (**a**) porosity P1 and (**b**) porosity P3.

6. Discussion

The performances of different heat-sink headers, evaluated with respect to the ability of generating a velocity distribution that is adequate for hotspot mitigation when using an

XF-DL-MCHS with 50 microchannels per layer for microchip thermal control, are compared with reference to the following parameters:

- the maximum normalized velocity difference at the two ends of the microchannel inlet sides, i.e., the difference between the normalized velocities in the last microchannel of a layer, u_{50}, and in the first microchannel of a layer, u_1

$$M_f = \frac{u_{50} - u_1}{u_{ave}} \tag{13}$$

- the mean deviation of the normalized microchannel velocities from a corresponding linear velocity distribution, which preliminary calculations showed to be the most effective to achieve a good temperature uniformity on the microchip surface

$$D_\ell = \frac{1}{50} \sum_{j=1}^{50} \left| \frac{u_j - u_{\ell,j}}{u_{ave}} \right| \tag{14}$$

In Equation (14), u_j is the velocity in the j-th microchannel and $u_{\ell,j}$ is the velocity in the same microchannel position in the case of a linear microchannel velocity distribution. For every actual velocity distribution u_j, velocities $u_{\ell,j}$ are calculated by imposing a linear trend that ensures the same flow rate and, at the same time, minimizes the mean velocity deviation $|u_j - u_{\ell,j}|$ from the actual distribution. As an example, Figure 12 shows the flow maldistribution profile for case S-L1 and $u_{ave} = 1.0$ m/s in red dots. The corresponding linear trend, in blue dots, ensures the same flow rate and is obtained by minimizing the mean distance between red and blue points for each microchannel.

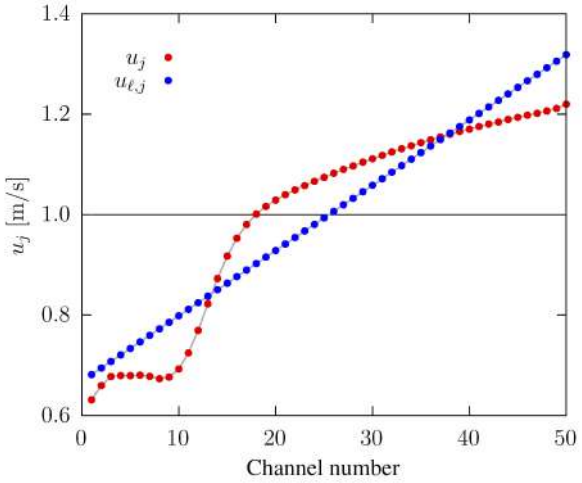

Figure 12. Velocity distribution u_j and corresponding linear velocity distribution $u_{\ell,j}$ for case S-L1 and $u_{ave} = 1.0$ m/s.

A large value of the flow maldistribution factor M_f means a high velocity in the microchannels farthest form the inlet port and a low velocity in the microchannels closest to the inlet port, with a positive effect on the hot spot control. A small value of D_ℓ means that the velocity distribution in the microchannel layer is close to a linear trend, that should also have a positive effect from the thermal point of view. Thus, for the purpose of this work, the higher the M_f and the lower the D_ℓ, the better it is. Both parameters have been calculated as the average of their values in the top and bottom microchannel layers.

In addition to the parameters M_f and D_ℓ, which measure how good a certain velocity distribution is from the hotspot control point of view, the pressure drop Δp in the MCHS also needs to be carefully considered. In this study, Δp is an overall pressure drop that includes losses in the inlet and outlet headers and in the microchannel layers, but not in the cylindrical inlet and outlet ports.

In Figure 13a,c,e, Δp is plotted against the maldistribution factor M_f for $u_{ave} = 0.5$, 1.0 and 2.0 m/s, respectively. The three charts show a nearly linear correlation between the pressure drop Δp and the maldistribution factor M_f pertaining to the different cases. For all values of u_{ave}, the headers without baffle (NB) exhibit the lowest pressure drops but also the lowest values of M_f. For all points, the larger the maldistribution factor the larger the pressure drop: the gray lines which connect points pertaining to cases with the same type of baffle (solid, cut, porous) have almost the same slope. Pressure losses are always higher than in the case without baffle, but are of the same order of magnitude and their maximum increase compared with the NB case goes from 28% for $u_{ave} = 0.5$ m/s to 51% for $u_{ave} = 2.0$ m/s. As expected, for the same header geometry M_f is much larger at high flow rates, meaning a more pronounced flow maldistribution. As an example, if we consider the case P2, M_f varies from 46% to 100% when u_{ave} goes from 0.5 to 2.0 m/s. Cut baffle cases have small maldistribution factors but not so little pressure drops: cases C2-L4 and S-L1 have almost the same value of M_f, but the pressure losses for the solid baffle case are smaller. Solid and porous baffle geometries present the largest values of M_f and not so different pressure drops Δp, especially at low flow rates. As far as these two parameters are concerned, it could be concluded that they have similar performance.

In Figure 13b,d,f, Δp is plotted against the mean deviation from a linear distribution D_ℓ for $u_{ave} = 0.5$, 1.0 and 2.0 m/s, respectively. The header without baffle (NB) always shows the lowest pressure drops, but some cut baffle configurations (C1-L4 and C1-L3, i.e., those with the smaller baffle height) show slightly lower values of D_ℓ. As in the case of M_f, for the same header geometry D_ℓ is larger at high flow rates, meaning a less linear-like trend. As an example, if we consider the case P2, D_ℓ varies from 0.036 to 0.045 when u_{ave} goes from 0.5 to 2.0 m/s.The largest values of this performance parameter are yielded by the solid baffle headers, especially for cases S-L2 and S-L3 (larger values of L_b) because, as explained in Section 5.2, velocity distributions feature peaks and valleys and are pretty far from a linear trend. In contrast to what happens with M_f, here the solid and the porous baffle geometries exhibit very different performances: although pressure drops are very similar, headers with porous baffles show much lower values of D_ℓ than headers with solid ones for all values of u_{ave}.

Comparing the results displayed in Figure 13a–f, it can be concluded that, for a given pressure drop, headers with porous baffles yield values of the maldistribution factor M_f similar to the ones that can be obtained with the other types of baffles, but for a given value of M_f, in almost all cases, the corresponding values of D_ℓ are lower than the others, meaning that velocity distributions in the microchannel layers are not too far from a linear one. The results in Figure 13 also show that by changing the permeability of the porous baffle a wide range of maldistribution factor M_f can be obtained while maintaining low values of D_ℓ. Finally, cut baffle headers yield very smooth microchannel velocity distributions, i.e., small values of D_ℓ, but limited velocity differences, i.e., small values of M_f, and could only be of interest if a mild maldistribution is sufficient for the hot spot control, for example at intermediate to high flow rates. All this demonstrates that, with an appropriate baffle selection, inlet headers of cross-flow MCHSs can yield microchannel velocity distributions that are close enough to those that would allow optimal hotspot management when heat sinks of this kind are used for the thermal control of electronic devices.

Although the effects of the flow maldistribution on the thermal field in cross-flow double-layered microchannel heat sinks will be the subject of a future study, some preliminary outcomes are reported here to highlight the usefulness of the findings of this work. An in-house finite element method (FEM) procedure [22,41] was used to carry out sample numerical simulations of the temperature and velocity fields in a MCHS with 50 microchannels as the one considered here with reference to the following conditions: $u_{ave} = 1.0$ m/s, $T_{in} = 300$ K, $q_w = 100$ W and heat sink made of silicon with thermal conductivity $k_s = 148$ W/(m K). Three microchannel velocity distributions were considered: a uniform distribution (the corresponding temperature field is the one already shown in Figure 2a), a linear distribution with $M_f = 0.7$ (the corresponding temperature field is

the one already shown in Figure 2b) and the velocity distribution of case P2, which is characterized by a value of M_f equal to 0.68, very similar to that of the linear distribution. Table 4 presents the maximum and minimum temperatures $T_{w,max}$ and $T_{w,min}$, the maximum temperature difference $\Delta T_{w,max}$ on the heated wall of the MCHS, the thermal resistance R_T and the percentage variations $\delta_{\Delta T_{w,max}}$ of $\Delta T_{w,max}$ and δ_{R_T} of R_T with reference to the uniform microchannel velocity case.

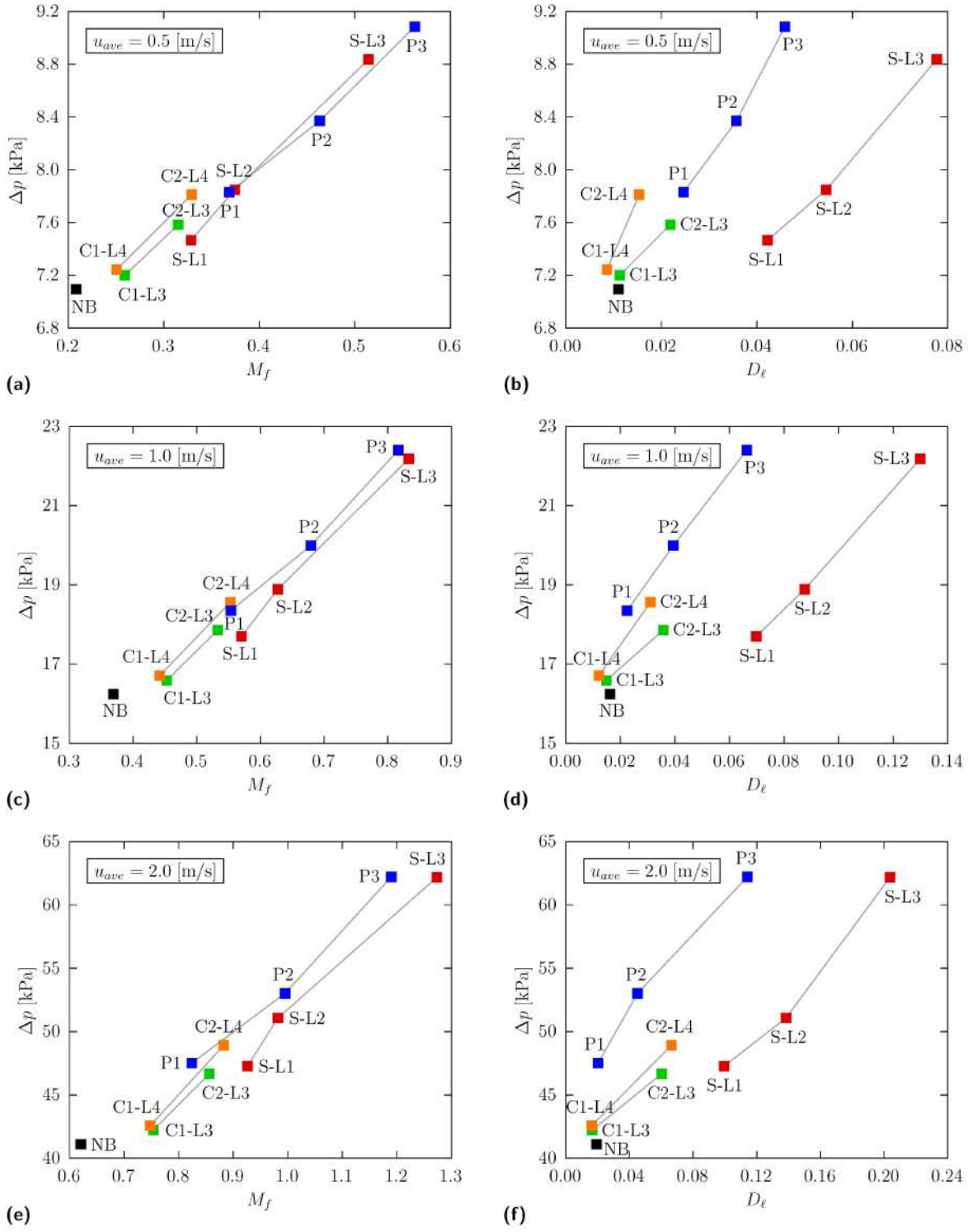

Figure 13. Performances of different heat-sink headers: (**a**,**c**,**e**) Δp vs. M_f and (**b**,**d**,**f**) Δp vs. D_ℓ, for different values of u_{ave}.

Table 4. Sample thermal performance of the MCHS for different microchannels velocity distributions and $u_{ave} = 1.0$ m/s.

Velocity Distribution	$T_{w,min}$ [K]	$T_{w,max}$ [K]	$\Delta T_{w,max}$ [K]	R_T [K/W]	$\delta_{\Delta T_{w,max}}$ [%]	δ_{R_T} [%]
Uniform ($M_f = 0$)	306.60	314.80	8.20	0.148	–	–
Linear ($M_f = 0.7$)	306.91	313.76	6.85	0.138	−16.5	−7.0
Case P2 ($M_f = 0.68$)	306.92	313.85	6.93	0.139	−15.6	−6.4

As can be seen, the maximum temperature difference $\Delta T_{w,max}$ and the thermal resistance R_T for the P2 case are very similar to those for the linear velocity distribution, and significantly lower than those yielded by the uniform microchannel velocity distribution.

7. Conclusions

The velocity field in the headers of cross-flow double-layered microchannel heat sinks was numerically investigated using the commercial code ANSYS Fluent. To reduce the computational effort, the flow in the microchannels of each layer was modeled as the flow in a porous material. Porous coefficients in the flow direction were calculated from pressure drop data in similar microchannels obtained using an in-house FEM code. Three values of the average microchannel velocity were considered: 0.5, 1.0 and 2.0 m/s. In addition to the basic geometrical configuration, several cases were analyzed in which a full or partial height baffle, solid or made of porous material, is inserted into the header. Results are presented in terms of pressure drop, maximum normalized velocity difference at the two ends of the microchannel inlet side and mean deviation of the microchannel inlet velocity distribution from a linear one. From the hotspot temperature control point of view, the higher the velocity difference and the lower the mean deviation from linearity, the better it is. Results of numerical simulations show that:

- solid baffle headers yield large velocity differences, but distributions far from a linear trend, while partial height baffle headers yield very smooth microchannel velocity distributions, but limited velocity differences;
- for a given pressure drop, headers with porous baffles yield values of the velocity difference similar to those obtained with the other types of baffles, but velocity distributions in the microchannel layers much closer to a linear trend;
- changing the permeability of the porous baffle, a wide range of velocity differences in the microchannel of a layer can be obtained, while maintaining very smooth velocity distributions.

We can conclude that, with a proper baffle selection, inlet headers of cross-flow microchannel heat sinks can yield velocity distributions very close to those that would allow optimal hotspot management in electronic devices. The effects of the flow maldistribution on the thermal field in cross-flow double-layered microchannel heat sinks will be the subject of a future study.

Author Contributions: Conceptualization, S.S. and C.N.; methodology, S.S. and C.N.; software, S.S.; validation, S.S., data curation, S.S. and C.N.; writing—original draft preparation, S.S. and C.N.; visualization, S.S. All authors have read and agreed to the published version of the manuscript.

Funding: The support of the MIUR through the PRIN Project 2017F7KZWS_005 on this research is gratefully acknowledged.

Conflicts of Interest: The authors declare no conflict of interest.

Abbreviations

The following abbreviations are used in this manuscript:

CF	Counter-flow
DL	Double-layered
FEM	Finite element method
FVM	Finite volume method
MCHS	Microchannel heat sink
RANS	Reynolds Averaged Navier-Stokes equations
XF	Cross-flow

References

1. Tuckerman, D.B.; Peas, R.F.W. High-performance heat sinking for VLSI. *IEEE Electron Device Lett.* **1981**, *2*, 126–129. [CrossRef]
2. Adham, A.M.; Mohd-Ghazali, N.; Ahmad, R. Thermal and hydrodynamic analysis of microchannel heat sinks: A review. *Renew. Sustain. Energy Rev.* **2013**, *21*, 614–622. [CrossRef]
3. He, Z.; Yan, Y.; Zhang, Z. Thermal management and temperature uniformity enhancement of electronic devices by micro heat sinks: A review. *Energy* **2021**, *216*, 119223. [CrossRef]
4. Vafai, K.; Zhu, L. Analysis of two-layered micro-channel heat sink concept in electronic cooling. *Int. J. Heat Mass Transf.* **1999**, *42*, 2287–2297. [CrossRef]
5. Wei, X.; Joshi, Y.; Patterson, M.K. Experimental and numerical study of a stacked microchannel heat sink for liquid cooling of microelectronic devices. *ASME J. Heat Transf.* **2007**, *129*, 1432–1444. [CrossRef]
6. Levac, M. L.-J.; Soliman, H. M.; Ormiston, S.J. Three-dimensional analysis of fluid flow and heat transfer in single- and two-layered micro-channel heat sinks. *Heat Mass Transf.* **2011**, *47*, 1375–1383. [CrossRef]
7. Hung, T.-C.; Yan, W.-M.; Li, W.-P. Analysis of heat transfer characteristics of double-layered microchannel heat sink. *Int. J. Heat Mass Transf.* **2012**, *55*, 3090–3099. [CrossRef]
8. Hung, T.-C.; Yan, W.-M.; Wang, X.-D.; Huang, Y.-X. Optimal design of geometric parameters of double-layered microchannel heat sinks. *Int. J. Heat Mass Transf.* **2012**, *55*, 3262–3272. [CrossRef]
9. Leng, C.; Wang, X.-D.; Wang, T.-H.; Yan, W.-M. Optimization of thermal resistance and bottom wall temperature uniformity for double-layered microchannel heat sink. *Energy Convers. Manag.* **2015**, *93*, 141–150. [CrossRef]
10. Wu, J.M.; Zhao, J.Y.; Tseng, K.J. Parametric study on the performance of double-layered microchannels heat sink. *Energy Convers. Manag.* **2014**, *80*, 550–560. [CrossRef]
11. Shen, H.; Xie, G.; Wang, C.C. Heat transfer and thermodynamic analysis by introducing multiple alternation structures into double-layer microchannel heat sinks. *Int. J. Therm. Sci.* **2019**, *145*, 105975. [CrossRef]
12. Chamoli, S.; Lu, R.; Chen, H.; Cheng, Y.; Yu, P. Numerical optimization of design parameters for a modified double-layer microchannel heat sink. *Int. J. Heat Mass Transf.* **2019**, *138*, 373–389. [CrossRef]
13. Zhou, J.; Hu, M.; Jing, D. An efficient method for the geometric parameters optimization of double-layer micro-channel heat sink. *Numer. Heat Transf. Part A* **2020**, *77*, 966–980. [CrossRef]
14. Patel, N.; Mehta, H.B. Experimental investigations on a variable channel width double layered minichannel heat sink. *Int. J. Heat Mass Transf.* **2021**, *165*, 120633. [CrossRef]
15. Zhang, Y.D.; Chen, M.R.; Wu, J.H.; Hung, K.S.; Wang, C.C. Performance improvement of a double-layer microchannel heat sink via novel fin geometry—A numerical study. *Energies* **2021**, *14*, 3585. [CrossRef]
16. Wang, T.H.; Wu, H.C.; Meng, J.H.; Yan, W.M. Optimization of a double-layered microchannel heat sink with semi-porous-ribs by multi-objective genetic algorithm. *Int. J. Heat Mass Transf.* **2020**, *149*, 119217. [CrossRef]
17. Li, X.Y.; Wang, S.L.; Wang, X.D.; Wang, T.H. Selected porous-ribs design for performance improvement in double-layered microchannel heat sinks. *Int. J. Therm. Sci.* **2019**, *137*, 616–626. [CrossRef]
18. Ghahremannezhad, A.; Vafai, K. Thermal and hydraulic performance enhancement of microchannel heat sinks utilizing porous substrates. *Int. J. Heat Mass Transf.* **2018**, *122*, 1313–1326. [CrossRef]
19. Ansari, D.; Kim, K.-Y. Double-layer microchannel heat sinks with transverse flow configurations. *ASME J. Heat Transf.* **2016**, *138*, 031005. [CrossRef]
20. Ansari, D.; Kim, K.-Y. Performance analysis of double-layer microchannel heat sinks under non-uniform heating conditions with random hotspots. *Micromachines* **2017**, *8*, 54. [CrossRef]
21. Tang, S.; Zhao, Y.; Quan, Z. Multi-objective optimization of double-layered microchannel heat sink based on derivative-free algorithm. *Numer. Heat Transf. Part A* **2018**, *73*, 535–552. [CrossRef]
22. Nonino, C.; Savino, S. Temperature uniformity in cross-flow double-layered microchannel heat sinks. *Fluids* **2020**, *5*, 143. [CrossRef]
23. Nonino, C.; Savino, S. Effects of Non-Uniform Flow Distribution In Double-Layered Cross-Flow Microchannel Heat Sinks. In Proceedings of the Second Pacific Rim Thermal Engineering Conference, Maui, HI, USA, 13–17 December 2019; Paper No. PRTEC-24191.

24. Mohammadi, M.; Jovanovic, G.N.; Sharp, K.V. Numerical study of flow uniformity and pressure characteristics within a microchannel array with triangular manifolds. *Comput. Chem. Eng.* **2013**, *52*, 134–144. [CrossRef]
25. Ghnai, I.A.; Sidik, N.A.C.; Kamaruzzaman, N.; Yahya, W.J.; Mahian, O. The effect of manifold zone parameters on hydrothermal performance of micro-channel HeatSink: A review. *Int. J. Heat Mass Transf.* **2017**, *109*, 1143–1161. [CrossRef]
26. Nonino, C.; Savino, S. Flow Maldistribution Effects on the Temperature Uniformity in Double-Layered Microchannel Heat Sinks. In Proceedings of the ASME 2019 17th International Conference on Nanochannels, Microchannels, and Minichannels, St. John's, NL, Canada, 23–26 June 2019.
27. Shih, T.H.; Liou, W.W.; Shabbir, A.; Yang, Z.;Zhu, J. A new $k-\epsilon$ eddy viscosity model for high reynolds number turbulent flows. *Comput. Fluids* **1995**, *3*, 227–238. [CrossRef]
28. ANSYS, Inc. *ANSYS Fluent User's Guide, Release 17.0*; ANSYS, Inc.: Canonsburg, PA, USA, 2016.
29. ANSYS, Inc. *ANSYS Fluent Theory Guide, Release 17.0*; ANSYS, Inc.: Canonsburg, PA, USA, 2016.
30. Hung, T.C.; Hung, Y.X.; Yan, W.M. Thermal performance of porous microchannel heat sink: effects of enlarging channel outlet. *Int. Commun. Heat Mass Transf.* **2013**, *48*, 86–92. [CrossRef]
31. Singh, R.; Akbarzadeh, A.; Mochizuki, M. Sintered porous heat sink for cooling of high-powered microprocessors for server applications. *Int. J. Heat Mass Transf.* **2009**, *52*, 2289–2299. [CrossRef]
32. Li, F.; Ma, Q.; Xin, G.; Zhang, J.; Wang, X. Heat transfer and flow characteristics of microchannels with solid and porous ribs. *Appl. Therm. Eng.* **2020**, *178*, 115639. [CrossRef]
33. Nonino, C.; Del Giudice, S.; Comini, G. Laminar forced convection in three-dimensional duct flows. *Numer. Heat Transf.* **1988**, *13*, 451–466.
34. Xie, G.; Li, S.; Sunden, B.; Zhang, W. Computational fluid dynamics for thermal performance of a water-cooled minichannel heat sink with different chip arrangements. *Int. J. Numer. Methods Heat Fluid Flow* **2014**, *24*, 797–810. [CrossRef]
35. Hempijid, M.; Kittichaikarn, C. Effect of heat sink inlet and outlet flow direction on heat transfer performance. *Appl. Therm. Eng.* **2020**, *164*, 114375. [CrossRef]
36. Ozsipahi, M.; Subasi, A.; Gunes, H.; Sahin, B. Numerical investigation of hydraulic and thermal performance of a honeycomb heat sink. *Int. J. Therm. Sci.* **2018**, *134*, 500–506. [CrossRef]
37. Chuan, L.; Wang, X.D.; Wang, T.H.; Yan, W.M. Fluid flow and heat transfer in microchannel heat sink based on porous fin design concept. *Int. Commun. Heat Mass Transf.* **2015**, *65*, 52–57. [CrossRef]
38. Hetsroni, G.; Gurevich, M.; Rozenblit, R. Sintered porous medium heat sink for cooling of high-power mini-devices. *Int. J. Heat Fluid Flow* **2006**, *27*, 259–266. [CrossRef]
39. Vafai, K. *Handbook of Porous Media*, 2nd ed.; Taylor & Francis: New York, NY, USA, 2005; pp. 212–213.
40. Lu, G.; Zhao, J.; Lin, L.; Wang, X.D; Yan, W.M. A new scheme for reducing pressure drop and thermal resistance simultaneously in microchannel heat sinks with wavy porous fins. *Int. J. Heat Mass Transf.* **2017**, *111*, 1071–1078. [CrossRef]
41. Nonino, C.; Savino, S. Numerical investigation on the performance of cross-flow micro heat exchangers. *Int. J. Numer. Methods Heat Fluid Flow* **2016**, *26*, 745–766. [CrossRef]